metals

MDPI

Article

Study on the Effect of Niobium on the High Temperature Oxidation Resistance of Ferritic Stainless Steel

En Zhu [1], Dianxiu Xia [1,*], Peidun Chen [2], Qing Han [1], Xuelin Wang [3], Zhiheng Liu [1] and Kun Jiang [1]

[1] School of Mechanical Engineering, University of Jinan, Jinan 250022, China; 202121100309@stu.ujn.edu.cn (E.Z.); me_hanq@ujn.edu.cn (Q.H.); 202121100308@stu.ujn.edu.cn (Z.L.); 202221201020@stu.ujn.edu.cn (K.J.)
[2] Shandong Taishan Iron and Steel Group Co., Ltd., Jinan 271100, China; tgcpd@126.com
[3] School of Materials Science and Engineering, University of Science and Technology, Beijing 100083, China; xuelin2076@ustb.edu.cn
* Correspondence: me_xiadx@ujn.edu.cn

Abstract: More and more cars are installing urea selective catalytic reduction (SCR) systems to solve the problem of exhaust emissions, which often operates at high temperatures in the exhaust system and is prone to failure of the exhaust pipe due to high-temperature oxidation. And niobium containing ferritic stainless steel has been widely used in the manufacturing of automotive exhaust pipes. In order to extend the service life of ferrite stainless steel exhaust pipes, niobium plays a crucial role as an added alloying element. The solid solution and precipitation of niobium in ferritic stainless steel will give ferritic stainless steel more excellent high temperature resistance. The precipitation of Nb can change the organizational structure in steel and refine the grains. However, if the content is not properly controlled, large particles of (Nb, Ti) C will precipitate, which will reduce the high temperature oxidation resistance. In this paper, the high temperature oxidation behavior of two kinds of ferritic stainless steels with different Nb content at 700 °C, 800 °C and 900 °C was studied. The microstructure of the oxide film on the surface of the material, the thickness of the oxide layer on the cross section, the distribution of chemical composition, the existence form and distribution of Nb element were analyzed by SEM, EDS, XRD and TEM. The results show that the higher the niobium content, the better the high temperature oxidation resistance, and the higher the temperature, the more obvious the high temperature oxidation resistance of niobium. This is because the high Nb content steel is easy to precipitate NbN and other Nb-containing precipitates at the grain boundary, which is helpful to the high temperature resistance. In the case of less Nb content, its ability to generate (Nb, Ti) C precipitates and coarsen at high temperatures reduces its high-temperature resistance.

Keywords: ferritic stainless steel; niobium; high-temperature oxidation; oxide film peeling; material failure; chromium diffusion

Citation: Zhu, E.; Xia, D.; Chen, P.; Han, Q.; Wang, X.; Liu, Z.; Jiang, K. Study on the Effect of Niobium on the High Temperature Oxidation Resistance of Ferritic Stainless Steel. *Metals* **2024**, *14*, 25. https://doi.org/10.3390/met14010025

Academic Editor: Pablo Pérez Zubiaur

Received: 13 September 2023
Revised: 14 December 2023
Accepted: 14 December 2023
Published: 25 December 2023

1. Introduction

In order to reduce pollution from automobile exhausts to the atmosphere, various countries have been continuously improving automobile exhaust emission standards in recent years. In order to meet the strict requirements of automobile exhaust emission standards, more and more commercial diesel vehicles have installed urea-selective catalytic reduction (SCR) exhaust aftertreatment devices. After installing the SCR exhaust aftertreatment device, the operating temperature of the automobile exhaust system is significantly increased, up to 900 °C, and more complications such as thermal expansion and contraction, thermal cycle and ammonia nitrogen atmosphere corrosion occur. The problem of exhaust system failure due to high-temperature oxidation is becoming more and more serious [1].

Previous studies have investigated nitrogen alloy austenitic stainless steel, which has increased mechanical properties (toughness, and tensile properties) and is used as a component material for automotive exhaust pipes [2]. Niobium-containing ferritic stainless steel

also has advantages such as high thermal conductivity, low thermal expansion coefficient, strong corrosion resistance, and lower manufacturing cost compared to austenitic stainless steel. Therefore, it is increasingly used as a raw material for exhaust pipes in SCR systems. Many researchers from China and other countries have studied the high-temperature oxidation behavior of ferritic stainless steel. Studies have shown that stainless steel often has better high-temperature stability after adding niobium [3]. It was found that the solid solution of Nb endows ferritic stainless steel with better high-temperature resistance, and the precipitation of Nb can change the solidification structure and refine the grains. But if the Nb content is not properly controlled, large particles of TiN and (Nb, Ti) (C, N) precipitate, reducing high-temperature performance. High-temperature oxidation failure is an important reason for the reduced service life or even failure and fracture of automotive exhaust system components equipped with SCR devices, leading to significant waste of resources and economic losses. Therefore, in-depth research on the effect of niobium on the high-temperature oxidation resistance of ferritic stainless steel is of great significance for improving the service life of automotive exhaust system components.

However, there is still a lack of in-depth research and more experimental data on the influence of niobium content on the high-temperature properties of niobium-containing ferritic stainless steel during high-temperature oxidation are needed. For example, Tianlong Liu et al. [4] studied 15CrNbTi ferritic stainless steel. The results show that there are three kinds of precipitated phases: (Nb, Ti) C phase, Fe_2Nb and Fe_3Nb_3 C; however, the effect of precipitated phases was not analyzed. Meng Qian et al. [5] conducted oxidation experiments at 800–1100 °C on two types of 310 s heat-resistant steels with different grain sizes and compositions. The results show that the smaller average grain size and more uniform grain size increase the diffusion flux of preferential oxidation elements and reduce the non-uniform growth of oxidation film. Mengqi Zhang et al. [6] and Badin et al. [7] studied the high-temperature oxidation behavior of ferritic stainless steel and found that its oxide layer consists of a small amount of SiO_2 and continuous dense Cr_2O_3, $FeCr_2O_4$, and Cr-Mn spinel oxides, which have high high-temperature oxidation resistance, but the oxidation mechanism has not been analyzed. Abdolvahid Movahedi-Rad et al. [8] studied the high-temperature oxidation behavior of 409 ferritic stainless steel. They believe that the Cr content of ferritic stainless steel is higher than that of austenitic stainless steel, and there is an internal oxidation zone rich in Cr in the oxidation layer. When sufficient Cr is provided, the penetration degree of the reaction front edge is higher.

This paper investigates the influence of niobium on high-temperature oxidation behavior, compares and studies the high-temperature oxidation behavior of two types of niobium-containing ferritic stainless steel, explores the effect of niobium content on the high-temperature oxidation resistance of ferritic stainless steel, and attempts to reveal the mechanism of niobium's effect on the high-temperature oxidation resistance of stainless steel.

2. Materials and Methods

2.1. Materials

The experimental materials were selected from two grades of ferrite stainless steel plates, 439 and 441, with a thickness of 3 mm (as shown in Table 1). For each experiment, 5 samples for each type of stainless steel were cut into blocks, then their surfaces were polished with 400 #, 800 #, 1200 #, 1500 #, and 2000 # sandpaper in sequence. Finally, they were mechanically polished to SPI (A2) polish grade.

Table 1. Main chemical composition of ferrite stainless steel (wt%).

	C	Si	Mn	P	Cr	Ni	Al	Nb	Ti	N
439	0.010	0.37	0.13	0.015	17.59	0.10	0.065	0.17	0.20	0.0084
441	0.010	0.39	0.23	0.016	18.00	0.10	0.037	0.41	0.16	0.0085

2.2. Methods

This experiment was conducted in the atmospheric environment of the laboratory. Three high-temperature oxidation temperatures were used: 700 °C, 800 °C, and 900 °C. An induction heater was used to heat the samples to temperature. They were kept warm for 30 min, and then cooled for 10 min to room temperature to form one cycle. Each type of sample was heated 30 times. After high-temperature oxidation, the sample was ultrasonically cleaned and stored in a drying dish, and then the composition of the oxide film was analyzed using X-ray diffraction (XRD). The microstructure of the oxide layer of the sample was analyzed using scanning electron microscopy (SEM), and its microstructure was analyzed using energy dispersive spectroscopy (EDS). Then the high-temperature oxidized samples were cold cut, and the surface of the samples in the cross-sectional direction was ground and polished to the same extent. The morphology, composition, and precipitation phase distribution of the oxide film and matrix at the cross-section was analyzed using SEM and XRD, and the precipitation of micro particles in the structure was observed using a transmission electron microscope (TEM). Typical positions of the samples were used for characterization, and the test results have generalizability.

3. Results

3.1. Surface High-Temperature Oxidation Morphology of Experimental Materials at Different Temperatures

The macroscopic and SEM morphology of the sample surface after oxidation of two types of stainless steel at different oxidation temperatures are shown in Figures 1–3. SEM figures with typical features were selected from 5 samples for each type of stainless steel in the article. Figure 1a,d show the macroscopic morphology of the oxidized surfaces of two materials after oxidation at 700 °C. It can be observed that there is still a significant metallic luster, indicating that there are still unoxidized parts or very thin oxide layers on the surfaces of the two materials at this temperature. When the oxidation temperature increased to 800 °C, the metallic luster on the 439 stainless steel sample disappeared and a complete oxidation layer appeared, as shown in Figure 1b. The oxidation layer on the 441 stainless steel sample is relatively complete, but some metallic luster remains, as shown in Figure 1e. As the oxidation temperature continued to rise to 900 °C, the surfaces of the two samples showed almost no metallic luster, were completely covered by the oxide layer, and the oxide layer turned black, indicating an increase in thickness of the oxide layer, and some highlighted areas indicated detachment of the oxide layer.

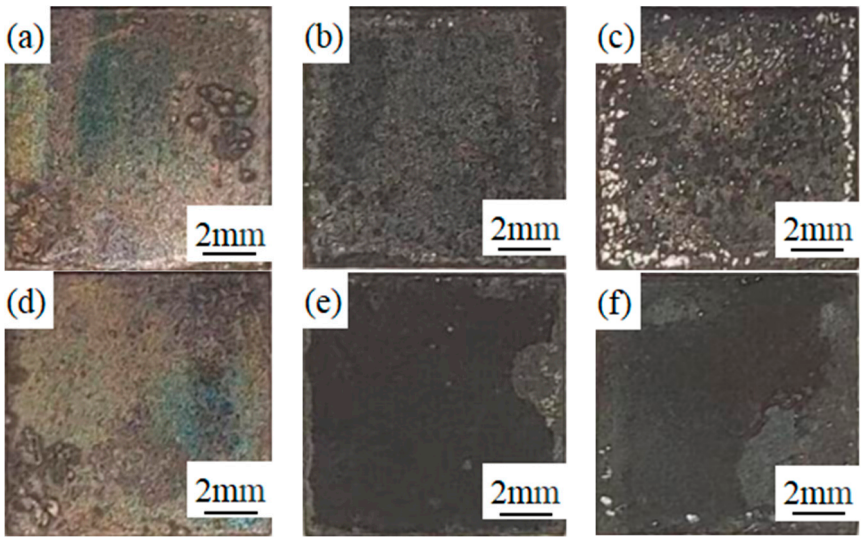

Figure 1. Macromorphology of high-temperature oxidation of samples at different temperatures (**a**) 700 °C (439), (**b**) 800 °C (439), (**c**) 900 °C (439), (**d**) 700 °C (441), (**e**) 800 °C (441), (**f**) 900 °C (441).

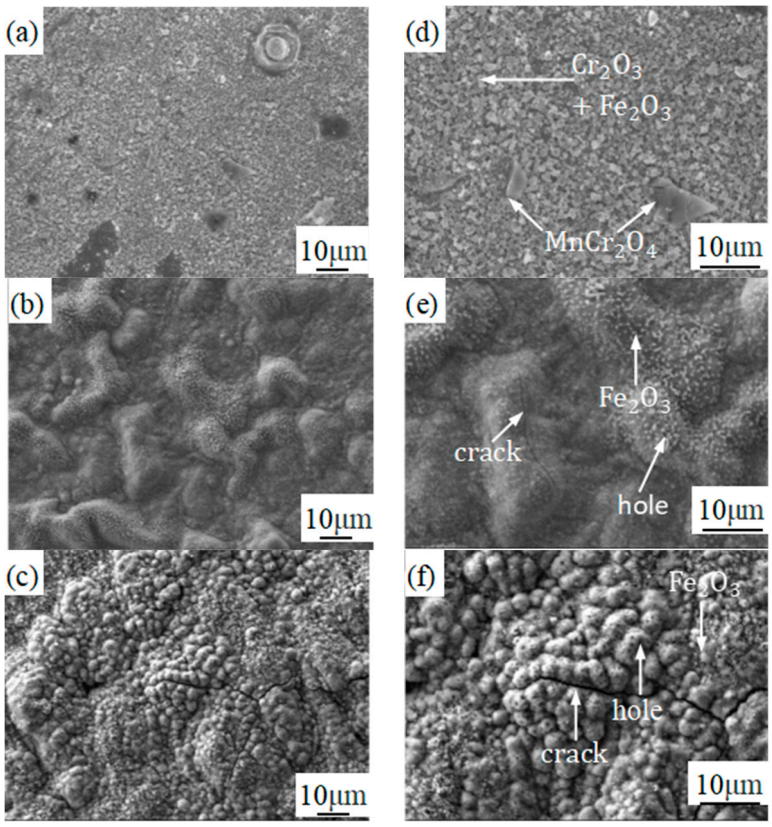

Figure 2. SEM morphology of 439 ferritic stainless steel during high temperature oxidation at different temperatures (**a**,**d**) 700 °C, (**b**,**e**) 800 °C, (**c**,**f**) 900 °C.

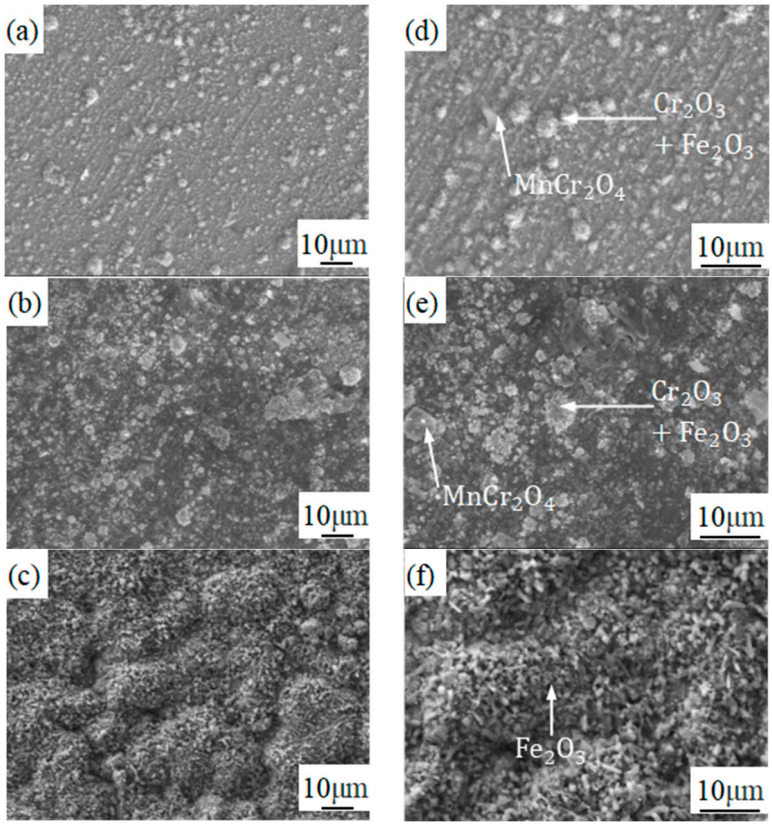

Figure 3. SEM morphology of high-temperature oxidation of 441 ferritic stainless steel at different temperatures (**a**,**d**) 700 °C, (**b**,**e**) 800 °C, (**c**,**f**) 900 °C.

Figure 2 shows the surface oxidation microstructure (SEM) of 439 stainless steel samples. From Figure 2a,d, it can be seen that after oxidation at a temperature of 700 °C, the 439 sample's surface forms small and densely packed oxide particles, with dense and layered oxidation products. It can be observed that there are also large spinel-like particles on the surface. As shown in Figure 2b,e, the number of surface granular oxides significantly decreases and accumulates together after oxidation at a temperature of 800 °C. Needle-like structures appear on the oxide shell layer (Figure 2e), which significantly reduces the protective effect of the substrate. In the experiment, thermal cycling generates internal stress, which can lead to surface cracking due to the different levels of hardness of various phases on the surface of the oxide layer. Pores appear on the oxide layer, allowing direct contact with unprotected collectives through the external environment of the pores, accelerating the internal oxidation process [4]. The morphology after oxidation at a temperature of 900 °C is shown in Figure 2c,e. The oxide layer rapidly grows and exhibits oxidation instability. The surface of the oxide tumor is composed of large spherical oxide particles, presenting a convex shape, and the surface of the spherical oxide is filled with holes, accompanied by cracks around it.

Figure 3 shows the surface oxidation microstructure (SEM) of 441 stainless steel sample. It can be seen that after oxidation at a temperature of 700 °C, surface granular oxides mainly aggregate in the form of large particles on a small scale, and gradually grow into small clusters on local surfaces. Most of the substrate passivation films have good integrity (Figure 3a,d). As the oxidation temperature rises to 800 °C, large particle oxides on the surface of the sample begin to grow into layered oxide films that accumulate on the substrate surface (Figure 3b,e). When the oxidation temperature rises to 900 °C, there is a significant change in the surface morphology of the sample, with needle-like oxidation nodules appearing on the surface but no cracking (Figure 3c,e). This is similar to the findings of Jacob et al., which indicate that the smaller the oxide particles, the greater the plasticity of the oxide layer, resulting in stronger adhesion between the oxide layer and the matrix [9].

As the oxidation temperature increases, the surface oxidation of both materials becomes increasingly severe.

3.2. Analysis of Oxide Layer Thickness of Experimental Materials at Different Temperatures

In order to further analyze the structure of the oxide layer, SEM characterization was performed on the cross-section of the sample oxide layer, and the thickness of the oxide layer was measured (Figures 4–6). The measured thickness of the oxide layer during characterization represents the thickest visible part of the oxide layer on the sample. The large dispersion of thickness measurements may be due to the different expansion coefficients of the matrix and the oxide during the cooling process, resulting in rupture, shedding or spalling.

From Figure 4, it can be seen that with the increase of temperature, the thickness of the oxide film on the surface of the sample gradually increases. From 800 °C to 900 °C, the oxide layer of stainless steel increases greatly, which generally conforms to the Arrhenius relationship [10]. The thickness of the oxide layer of 439 stainless steel is greater than that of 441 stainless steel at three temperatures, especially at 900 °C, and the error bar in Figure 5 shows that the thickness inhomogeneity of the oxide layer on 439 stainless steel is also greater than that of 441 stainless steel. The data show that the thickness of the oxide layer is not much different between the two at 700 °C. But when oxidized at 800 or 900 °C, the thickness of the oxide layer of 439 stainless steel is almost twice that of 441 stainless steel, indicating that the higher the temperature, the more obvious the high-temperature oxidation resistance of niobium [11].

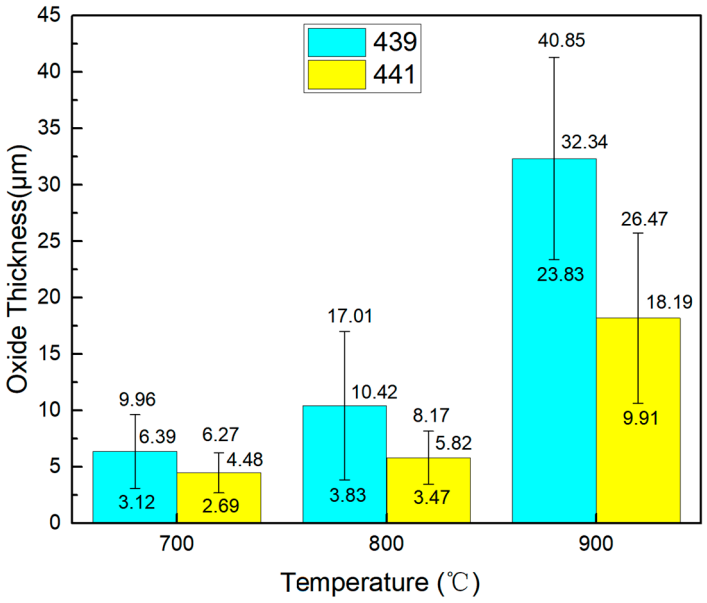

Figure 4. Thickness of two types of ferrite oxide layers at different temperatures.

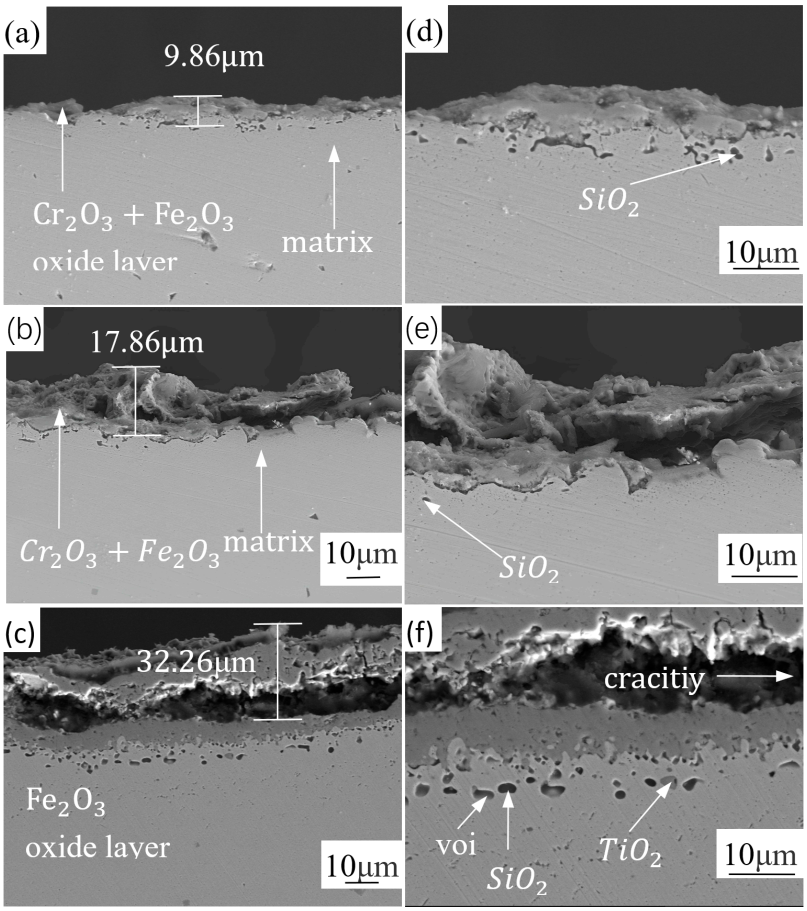

Figure 5. SEM morphology of 439 stainless steel at the interface between substrate and oxide layers at different temperatures (**a**,**d**) 700 °C, (**b**,**e**) 800 °C, (**c**,**f**) 900 °C.

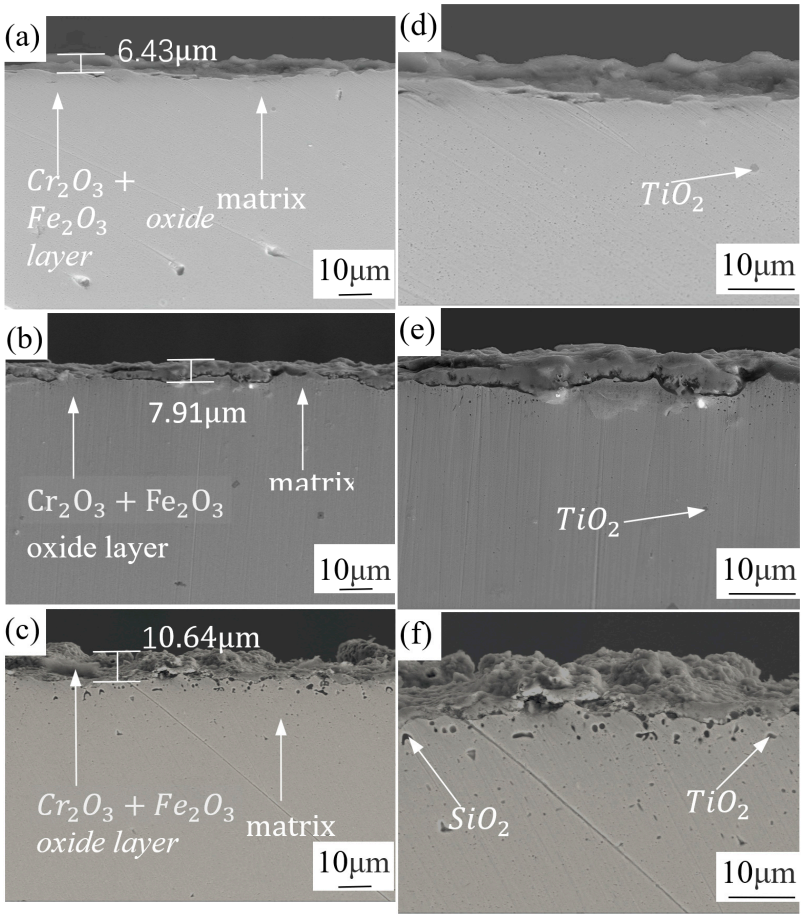

Figure 6. SEM morphology of 441 stainless steel at the interface between substrate and oxide layers at different temperatures (**a**,**d**) 700 °C, (**b**,**e**) 800 °C, (**c**,**f**) 900 °C.

Comparing the oxidation cross-sections of two types of stainless steel, the oxide layer thickness of 441 stainless steel is smaller than that of 439 stainless steel, and the integrity of the oxide layer is better, reflecting that 441 stainless steel has stronger high-temperature oxidation resistance than 439 stainless steel. In addition, comparing Figure 5f with Figure 6f, it can be found that SiO_2 particles are generated between the surface of the oxidation layer and metal matrix after oxidation at 900 °C. However, the size and density of the SiO_2 particles in 439 steel are greater than those of 441 steel. Research has shown that the SiO_2 layer can block the diffusion of oxygen to the matrix metal, so the more severe inward oxidation of 439 results in more SiO_2 particles generated at high temperatures than in 441 stainless steel [12].

Oxygen can penetrate into the stainless steel matrix, and Ti and Si that were originally dissolved near the surface of the stainless steel can combine with oxygen to generate TiO_2 and SiO_2. This makes the concentration of Ti and Si solution decrease. Under increased diffusion ability of the crystal interface at high temperature, according to Fick's first law, Ti and Si inside the matrix begin to diffuse towards the oxide film, and a large number of TiO_2 and SiO_2 particles are generated near the junction of the matrix and the oxide film. Finally, voids are formed around the particles due to the Kirkendall effect.

3.3. Analysis of Composition Distribution and Phase Structure of the Oxidized Surface at Different Temperatures

In order to study phase changes during high-temperature oxidation, EDS was used to scan the oxidized surface to analyze elemental distribution (Figures 7 and 8), and XRD phase composition analysis was performed on the oxidized surface (Figure 9).

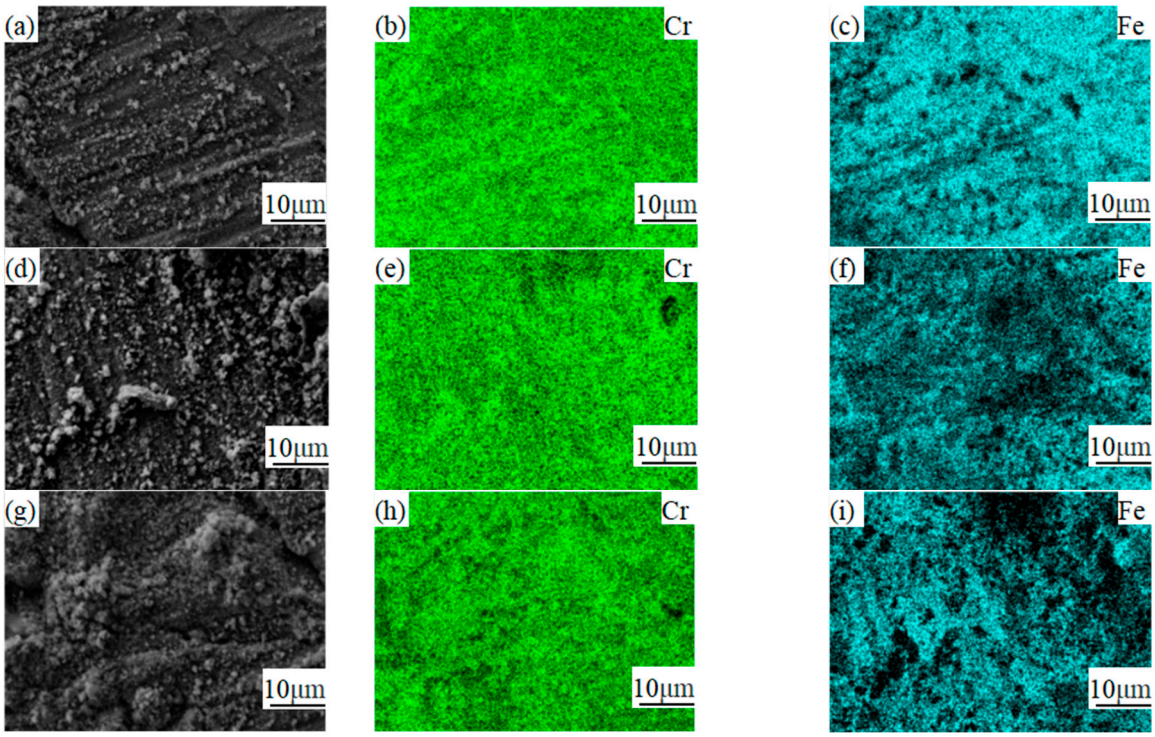

Figure 7. Element distribution on 439 high-temperature oxidation surface at different temperatures (EDS surface scanning) (**a**) 700 °C-morphology, (**b**) 700 °C-Cr, (**c**) 700 °C-Fe, (**d**) 800 °C-morphology, (**e**) 800 °C-Cr, (**f**) 800 °C-Fe, (**g**) 900 °C-morphology, (**h**) 900 °C-Cr, (**i**) 900 °C-Fe.

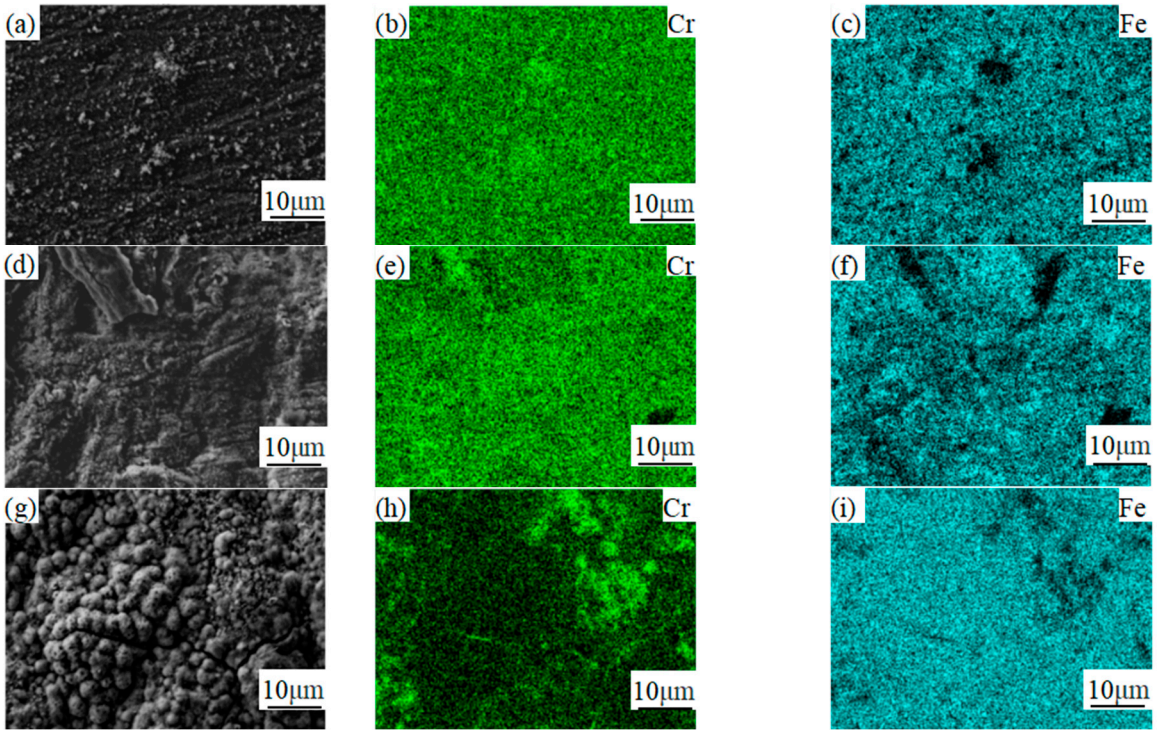

Figure 8. Element distribution on 441 high-temperature oxidation surface at different temperatures (EDS surface scanning) (**a**) 700 °C-morphology, (**b**) 700 °C-Cr, (**c**) 700 °C-Fe, (**d**) 800 °C-morphology, (**e**) 800 °C-Cr, (**f**) 800 °C-Fe, (**g**) 900 °C-morphology, (**h**) 900 °C-Cr, (**i**) 900 °C-Fe.

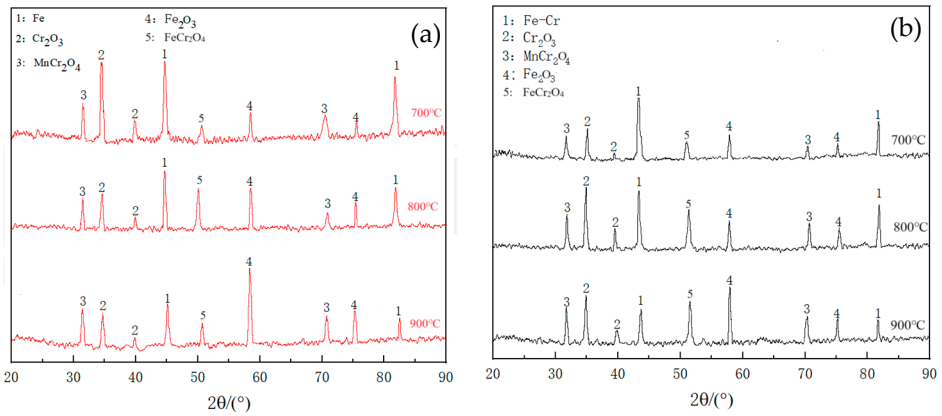

Figure 9. XRD spectra of oxidation products on the surface of two types of stainless steel after high-temperature oxidation (**a**) 439, (**b**) 441.

Figure 7 shows the distribution of oxidation surface composition of 439 stainless steel. From Figures 7b,e and 9, it can be seen that the oxidation layer of 439 stainless steel in the early stage of oxidation is mainly composed of Cr_2O_3. When the temperature increases from 700 °C to 800 °C, the distribution of the Cr element does not change significantly. Based on Figure 9a, it can be seen that the surface of the oxide layer is mainly composed of Cr_2O_3 and Fe_2O_3, but the specific morphology of the oxide layer is different. But when the oxidation temperature rises to 900 °C (Figure 7h), surface Cr rapidly decreases, and it is analyzed together with the experimental data in Figure 9a, only Fe_2O_3 remains on the surface oxide layer. The specific composition of the oxide layer is Fe_2O_3 and Cr_2O_3, mainly controlled by the diffusion of Cr element towards the surface layer of the matrix [13]. When 439 stainless steel is oxidized at a temperature of 900 °C, the Cr content on the oxidized surface significantly decreases, and the Cr element on the surface escapes from the oxide layer through the following reactions [14]:

$$Cr_2O_3(s) + \frac{3}{2}O_2(g) = 2CrO_3(g) \quad (1)$$

The generated CrO_3 is prone to volatilization at high temperatures, so the Cr_2O_3 and Fe_2O_3 mixed solid oxide layer that should have been generated only leaves a shell of Fe_2O_3. Solid Cr_2O_3 in the mixture is transformed into a gaseous CrO_3, which evaporates from pores in the shell, as shown in Figure 2e. At the same time, the hollow shell structure is more prone to cracking under internal stress.

By analyzing the specific composition of the oxide layer based on the XRD spectrum in Figure 9, it can be seen that when the oxidation temperature is 700 °C, the oxidation products of 439 stainless steel, except for the mixed oxide layer composed of Cr_2O_3 and Fe_2O_3, contain $MnCr_2O_4$ spinel particles in the oxide layer. The oxide film generated at lower temperatures is relatively thin, and Fe and Cr in the matrix are also detected. The two exist in a solid solution manner in the collective, making it difficult to distinguish them. After the temperature rises to 800 °C, an increase in surface oxide film thickness can be observed at the macro level, while an increase in Cr_2O_3 peak intensity at the micro level indicates that the oxide film generated by 439 stainless steel is thicker. In addition to the increase in thickness of the oxide layer, some areas exhibit a Fe_2O_3 shell structure during sintering, resulting in an increase in the overall Fe_2O_3 peak strength. Moreover, during the oxidation cycle, the oxide layer is prone to cracking and peeling due to thermal stress, and the protective ability of the matrix is lost in these areas. When the Cr element is sufficient, the cracked and peeled parts regenerate an oxide film, resulting in an overall increase in content. In addition to Cr_2O_3, it can also lead to oxidation of the matrix to form Fe_2O_3 or other oxides. As the oxidation temperature rose to 900 °C, the Cr_2O_3 component in the oxide film decreased significantly, while the iron oxide Fe_2O_3 increased significantly. Stainless steel can protect the substrate by adhering Cr_2O_3 on its surface in non-high-

temperature working environments. However, under high temperature conditions such as 900 °C in this experiment, Cr_2O_3 will react with oxygen, resulting in CrO_3, which is a volatile oxide at high temperatures [15]. In this experiment, due to the transformation of 439 stainless steel during oxidation at 900 °C, the CrO_3 volatilization generated by the oxide layer significantly reduced the surface Cr content (Figure 7h). This allows the external environment to come into contact with the substrate through the generated pores, providing a way for further inward oxidation [16].

The EDS spectra of 441 stainless steel show little difference from 439 stainless steel at 700 °C and 800 °C, but there is a significant difference at 900 °C. The surface has a higher Cr content and a lower Fe content. The reason is that 439 stainless steel experienced a significant loss of Cr on the reaction surface, resulting in iron element in the oxide layer increased covering the surface [17]. However, 441 stainless steel did not undergo this reaction, so there is still a mixed iron chromium oxide layer on the surface. According to the XRD phase analysis in Figure 9, it can be seen that there are fewer oxidation products on the surface of 441 stainless steel compared to 439 stainless steel at an oxidation temperature of 700 °C. In Figure 9a,b, the oxidation does not clearly reflect the stronger high-temperature oxidation resistance of 441. However, in Figure 9c, the content of Cr_2O_3 in 441 is actually higher than that in 439, indicating a significant loss of Cr on the surface of 439 and the loss of the protective ability of the oxide layer.

According to the XRD phase analysis of two types of stainless steel cross-sections in Figure 10, the main reason for the different morphology of the oxide layer is the effect of niobium element. Niobium can refine ferrite grains [18]. From Figure 10a at 700 °C, Figure 10b at 800 °C, and Figure 10c at 900 °C, it can be observed that the content of Cr_2O_3 decreases, while the content of Fe_2O_3 increases, and the change in 439 stainless steel is more significant than that in 441 stainless steel. To enable the oxide layer to protect the substrate, it is necessary to ensure the stable growth of Cr_2O_3 during the oxidation process. It is necessary to ensure that the chromium flux diffused from the substrate to the oxide interface is greater than the chromium flux diffused from the oxide film to the outside. Otherwise, it is easy to cause chromium depletion. The Cr_2O_3 reaction in the Cr_2O_3, Fe_2O_3 and TiO_2 mixed oxide layer is depleted, resulting in voids like Figure 7c. At this point, the chromium content supplied by the matrix is insufficient, so Cr_2O_3 cannot be formed again on the matrix without oxide layer protection in the cavity, and the matrix will directly participate in oxidation [19].

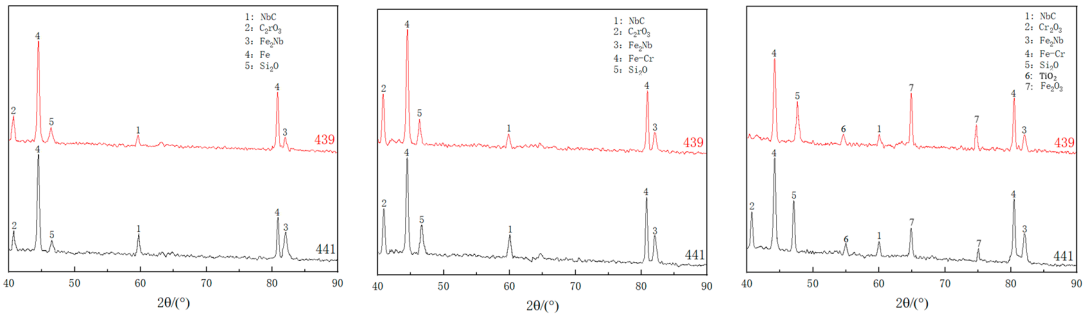

(**a**) (**b**) (**c**)

Figure 10. XRD phase analysis of high-temperature oxidation cross-sections of ferritic stainless steel at different temperatures (**a**) 700 °C, (**b**) 800 °C, (**c**) 900 °C.

In order to analyze the impact of precipitates on the resistance to high-temperature oxidation performance, typical morphologies of precipitates in two samples, Figures 11 and 12, were observed using TEM. According to the morphology and energy spectrum analysis of the precipitates, it can be determined that the precipitates in the 439 sample with low niobium content are mainly composed of (Nb, Ti) C composite precipitates within the crystal. The size is relatively large; the diameter of precipitates ranges from 2 to 3 μm;

however, no large particles were found in the 441 sample with a higher niobium content. Compared to the precipitates in 439 stainless steel, the precipitates on the grain boundaries of 441 stainless steel are finer; the diameter of precipitates ranges from 100 to 200 nm. As shown in Figure 12b–d, the composition of the precipitates includes Nb and Ti instead of C, which can be inferred as (Nb, Ti) N composite precipitation. Due to the low content of N and the difficulty of scanning N elements, this elemental energy spectrum appears [20].

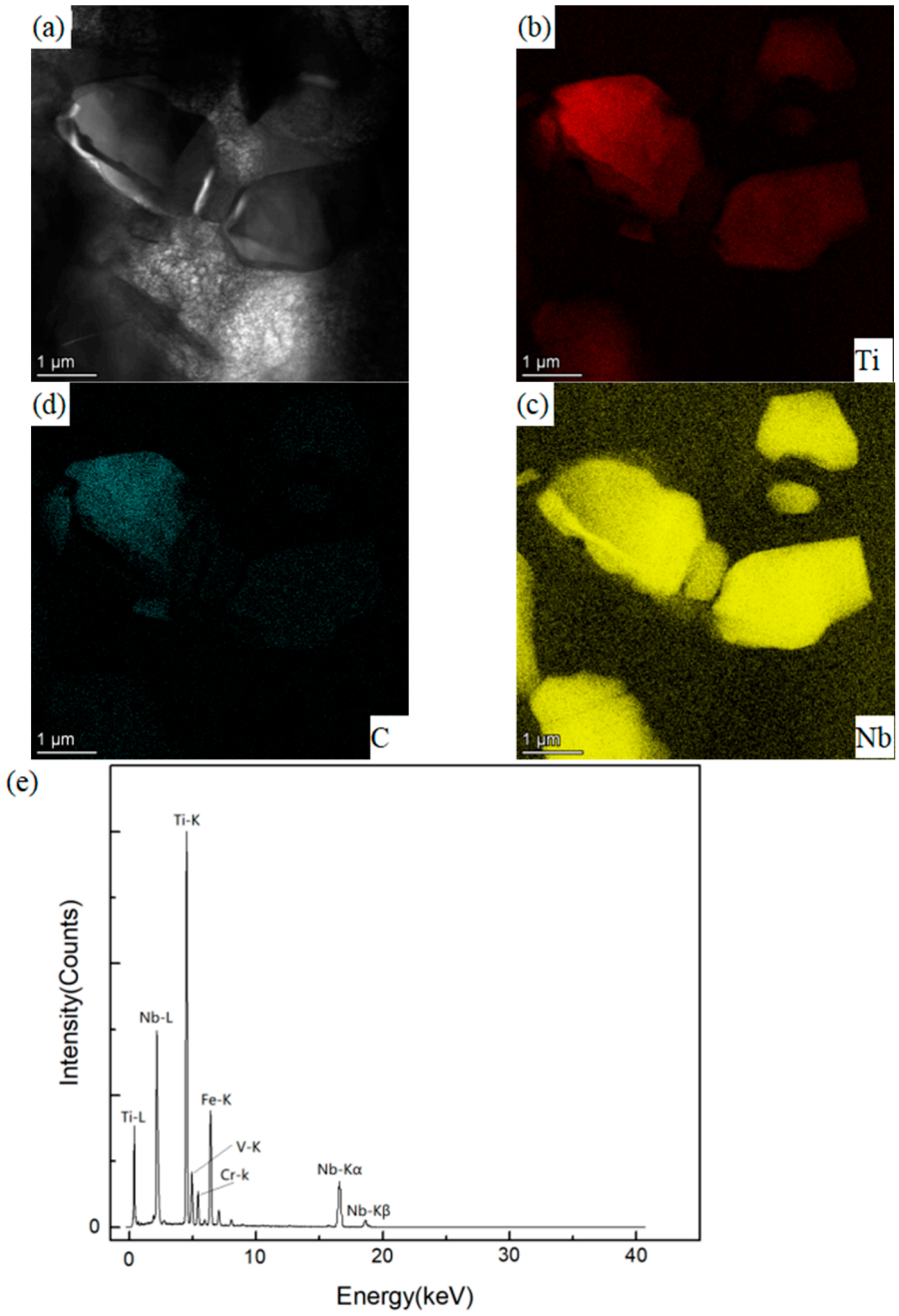

Figure 11. TEM morphology and elemental analysis of 439 stainless steel precipitates after oxidation at 900 °C (**a**) TEM morphology map; (**b**) Ti elemental energy spectrum; (**c**) energy spectrum of Nb element; (**d**) C element energy spectrum; (**e**) elemental spectrogram.

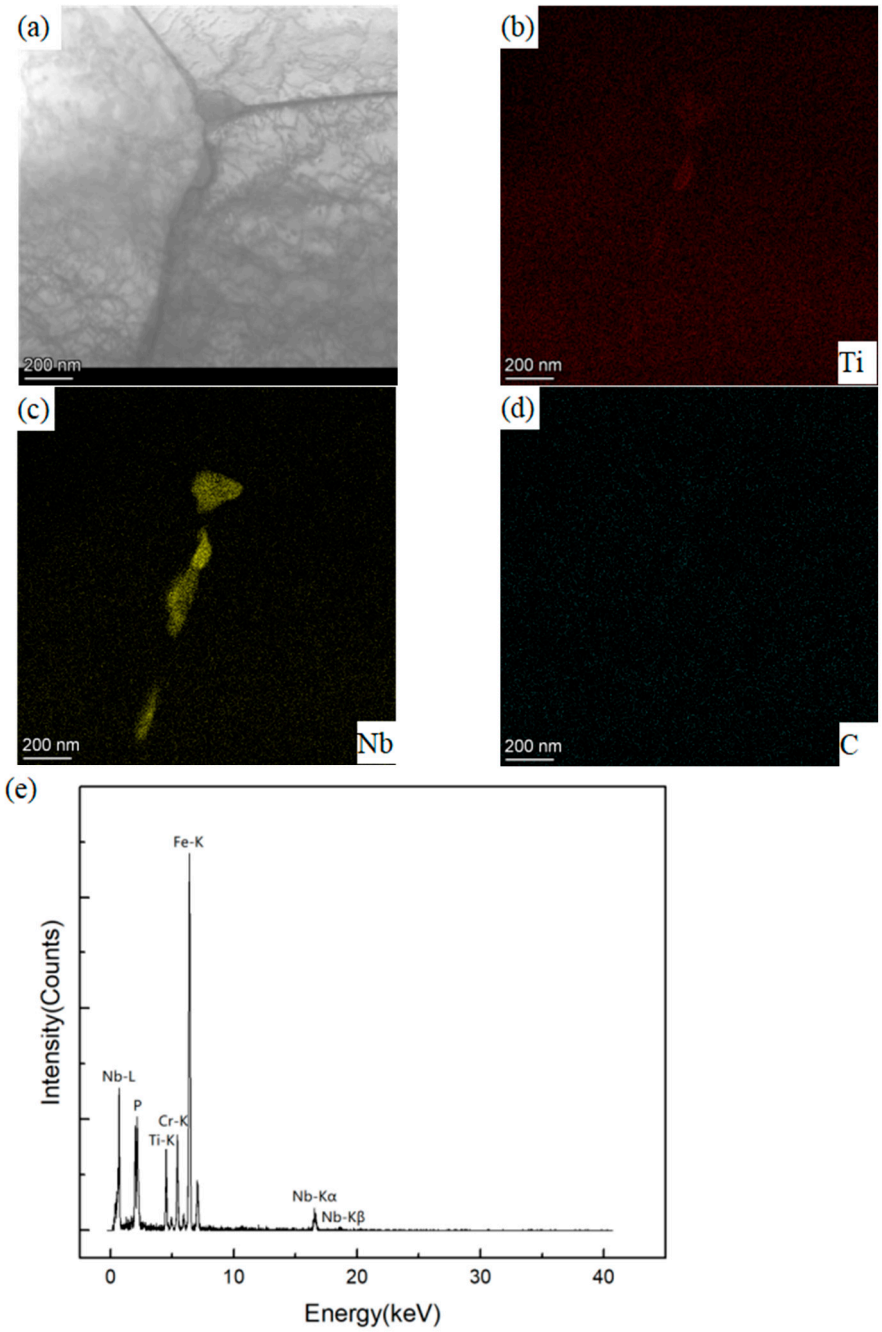

Figure 12. TEM morphology and elemental analysis of 441 stainless steel precipitates after oxidation at 900 °C (**a**) TEM morphology map; (**b**) Ti elemental energy spectrum; (**c**) energy spectrum of Nb element; (**d**) C element energy spectrum; (**e**) elemental spectrogram.

As shown in Table 1, 439 stainless steel has a high content of Ti and Al. Due to the higher precipitation temperature of TiN and AlN compared to NbN during melting, TiN and AlN precipitate before NbN and consume most of the N element. Therefore, Nb elements in 439 stainless steel are more likely to form NbC composite precipitates. In 441 stainless steel, the initial precipitation of TiN provides nucleation for NbN precipitation, resulting in (Nb, Ti) N composite precipitation.

4. Discussion

During the oxidation process, Gibbs free energy decreases with the increase of temperature, and the decrease in interfacial free energy between carbides and the matrix promotes

the aggregation and growth of carbides [21]. On the other hand, the diffusion caused by the concentration difference between carbides and alloy elements in the matrix provides a dynamic driving force. Therefore, the 439 stainless steel before the high-temperature oxidation experiment did not exhibit 2–3 properties as shown in Figure 10a μm long (Nb, Ti) C composite precipitates. However, during high-temperature oxidation, the carbides undergo coarsening as the temperature increases.

Before high-temperature oxidation, the average particle size of precipitates is balanced locally between particles and crystals at the boundary of precipitates. When high-temperature oxidation occurs, Gibbs free energy decreases with the increase of temperature, and large-sized precipitates have smaller Gibbs energy addition than average sized precipitates. In order to maintain the overall composition of the precipitates, the size of the precipitates will correspondingly increase [22].

However, no large particle precipitates were found in 441, and the precipitated fine NbN played a fixed role at the grain boundary after precipitation, thus preventing further grain growth and reducing the average grain size. Grain refinement improves the oxidation resistance of steel, reduces its oxidation weight gain, and delays the occurrence of unstable oxidation. The higher content of niobium in 441 stainless steel is more likely to combine with C and N, which to some extent prevents the combination of Cr element with N and C to generate CrN and Cr_3C_2 [23]. During high-temperature oxidation of stainless steel, it is easy to generate CrN and Cr_3C_2 deposits at grain boundaries, and the areas immediately adjacent to CrN will lose chromium elements and form chromium-deficient areas. If a chromium-deficient area appears, it will increase the activity of chromium elements near the area, leading to the loss of Cr element during high-temperature oxidation [24].

Firstly, during the initial process of oxidation, the stainless steel oxide film will begin to form pores or microcracks, leading to the growth of some oxide grains in the oxide film, resulting in the appearance of oxidized surface particles as shown in Figures 2a and 3a. When oxidized at high temperature, O element diffuses inward, and the solid-soluble Cr in the matrix will preferentially combine with O to form Cr_2O_3 [25]. When the content of Cr in the matrix is insufficient, O will combine with F to form Fe_2O_3, causing failure. By adding Nb to fix Cr, Nb will preferentially combine with N and C in steel to form Nb (N, C) and other precipitates, thus avoiding the decrease of the concentration of solid-soluble Cr in the matrix. As the temperature increases, the Cr_2O_3 layer in the oxidation layer of 439 stainless steel continuously evaporates, resulting in a large number of defects such as oxidation layer pores and cracks on the surface, leading to continuous inward oxidation. The speed of supplying Cr from the substrate to the oxide skin through diffusion is not fast enough to maintain a high Cr concentration in the oxide layer, and Fe is easily diffused outward, forming Fe-rich nodular oxides [26].

As mentioned above, no Nb-containing intergranular precipitates were found in the 439 steel as shown in Figure 12a, resulting in chromium-deficient areas. At high temperatures, the Cr element further reacts to generate volatile CrO_3, resulting in voids in the previous solid oxide layer caused by volatilization of CrO_3. Through the voids, the matrix can continue to come into contact with the external environment. Therefore, intense oxidation reactions will continue to occur near the chromium-rich area on the substrate, resulting in a thicker oxide layer on the side near the substrate in the cavity shown in Figure 4f.

Overall, the (Nb, Ti) C precipitates generated by 439 stainless steel will continue to grow during high-temperature oxidation, which is detrimental to the high-temperature performance of stainless steel [27]. The (Nb, Ti) N precipitates generated between grains in 441 stainless steel can play a role in pinning crystals to prevent grain coarsening during high-temperature oxidation and solidify Cr [28], so the high-temperature oxidation resistance of 441 stainless steel is superior to that of 439 stainless steel.

5. Conclusions

(1) As the oxidation temperature increases, the oxide layer of both types of stainless steel will increase. The oxide layer thickness of 441 stainless steel with higher niobium content is less than 439 stainless steel at the same temperature. The oxide layer of 441 stainless steel is intact at any temperature, while 439 stainless steel exhibits cracking and voids in the oxide layer at high temperatures.

(2) The phase structure composition and oxidation morphology of the oxide layer vary at different temperatures. When the sample is oxidized at 700 °C, the oxidation layer of both types of ferritic stainless steel are Cr_2O_3 and Fe_2O_3. The oxidation layer of 439 stainless steel is dense and uniform, while 441 stainless steel is a discrete oxide particle. When the sample is oxidized at 800 °C, the oxidation products on the surface of 439 stainless steel are sintered together, and needle-like Fe_2O_3 structures appear on the oxide film, while the oxidation particles on the surface of 441 stainless steel grow and aggregate into a uniform oxide layer. When the sample is oxidized at 900 °C, the oxidation layer exhibits internal and external layering, with an outer layer of Fe_2O_3 shell structure and an inner layer of iron-containing oxides such as Fe_2O_3, Fe_3O_4, and FeO. However, 441 stainless steel has a needle-like Fe_2O_3 oxidation tumor on its surface but no cracking occurs, indicating a relatively complete oxidation layer.

(3) The reason why 439 steel has poor high-temperature oxidation resistance is that (Nb, Ti) C precipitates coarsen at high temperatures, which has a destructive effect on high-temperature resistance. The reason why 441 steel has good high-temperature oxidation resistance is due to the precipitation of NbN and other niobium-containing precipitates at grain boundaries, which has the effect of refining grains and hindering the escape of Cr elements.

Author Contributions: Conceptualization, E.Z., D.X., P.C. and Q.H.; methodology, D.X.; validation, X.W., Z.L. and K.J.; investigation, D.X. and Z.L.; writing—original draft preparation, E.Z., D.X. and Q.H.; writing—review and editing, D.X.; project administration, D.X. and Q.H.; funding acquisition, P.C. All authors have read and agreed to the published version of the manuscript.

Funding: Shandong Provincial Natural Science Foundation, ZR2021ME247. Major R&D Plan Project in Shandong Province, 2023CXPT081.

Data Availability Statement: The data presented in this study are available on request from the corresponding author. As this paper is based on sponsored Funding, experimental data are used for the research and development of new ferritic stainless steel in Funding, so experimental data are not publicly available.

Conflicts of Interest: Author Peidun Chen was employed by the company Shandong Taishan Iron and Steel Group Co. The remaining authors declare that the research was conducted in the absence of any commercial or financial relationships that could be construed as a potential conflict of interest.

References

1. Oku, M. Development of Heat-resistant Ferritic Stainless Steel for Automotive Exhaust Systems Made by Nippon Steel. *World Steel* **2011**, *5*, 10–16.
2. Di Schino, J.M.; Barteri, K.M. High temperature resistance of a high nitrogen and low nickel austenitic stainless steel. *J. Mat. Sci. Lett.* **2003**, *22*, 691–693.
3. Dong, Z.; Chen, H.; Lang, Y. The effect of niobium and titanium on the high-temperature mechanical properties of ferritic stainless steel used in the hot end of automotive exhaust systems. *Steel* **2013**, *48*, 64–68.
4. Liu, T.; Chen, L.; Bi, H.; Che, X. Effect of Mo on High-Temperature Fatigue Behavior of 15CrNbTi Ferritic Stainless Steel. *Acta Metall. Sin. Engl. Lett.* **2014**, *27*, 452–456. [CrossRef]
5. Meng, Q.; Li, D.; Yang, J.; Liu, T. High temperature oxidation behavior of 310S heat-resistant steel. *Mater. Eng.* **2022**, *50*, 137–149.
6. Zhang, M.; Han, Y.; Zu, G.; Sun, J.; Zhu, W.; Chen, H.; Ran, X. High-Temperature Oxidation Behavior of a Cu-Bearing 17Cr Ferritic Stainless Steel. *Scanning* **2020**, *2020*, 8847831. [CrossRef]
7. Badin, V.; Diamanti, E.; Forêt, P.; Darque-Caretti, E. Characterization of oxide scales formed on ferritic stainless steel 441 at 1100 °C under water vapor. *Oxid. Met.* **2014**, *82*, 347. [CrossRef]
8. Movahedi-Rad, A.; Pelaseyed, S.S.; Attarian, M.; Shokrallahzadeh, R. Oxidation behavior of AISI 321, AISI 316, and AISI 409 stainless steels: Kinetic, thermodynamic, and diffusion studies. *J. Mater. Res.* **2016**, *31*, 2088–2096. [CrossRef]

9. Jacob, Y.P.; Haanappel, V.; Stroosnijder, M.F. The effect of gas composition on the isothermal oxidation behaviour of PM chromium. *Corros. Sci.* **2002**, *44*, 2027–2039. [CrossRef]
10. Raj, K.A. On High-Temperature Materials: A Case on Creep and Oxidation of a Fully Austenitic Heat-Resistant Superalloy Stainless Steel Sheet. *J. Mater.* **2013**, *2013*, 124649.
11. Cheng, L. Study on High Temperature Oxidation Behavior of Ferritic Stainless Steel. Ph.D. Thesis, Shenyang University, Shenyang, China, 2021.
12. Duan, X.; Zhang, J.; Zhang, S.; Li, G.; Wei, Y. The effect of Nb and Ti on the high-temperature oxidation behavior of 444 ultra pure ferrite stainless steel. *Spec. Steel* **2021**, *42*, 7–11.
13. Seo, H.S.; Yun, D.W.; Kim, K.Y. Oxidation behavior of ferritic stainless steel containing Nb, Nb-Si and Nb-Ti for SOFC interconnect. *Int. J. Hydrogen Energy* **2012**, *38*, 2432–2442. [CrossRef]
14. Safikhani, A.; Esmailian, M.; Tinatiseresht, T.; Darban, G.B.D. High temperature cyclic oxidation behavior of ferritic stainless steel with addition of alloying elements Nb and Ti for use in SOFCs interconnect. *Int. J. Hydrogen Energy* **2016**, *41*, 6045–6052. [CrossRef]
15. Haitao, Y.; Hongyun, B.; Xin, L.; Zhou, X. Precipitation and mechanical properties of Nb-modified ferritic stainless steel during isothermal aging. *Mater. Charact.* **2009**, *60*, 204.
16. Peng, J.; Li, M.; Luo, S. Study on high-temperature oxidation behavior of B443NT ferritic stainless steel. *Baosteel Technol.* **2013**, 22–25+31.
17. Huang, H.; Yang, Y. Study on high-temperature oxidation behavior of niobium titanium double stabilized 430 stainless steel. *J. Mater. Res.* **2014**, *28*, 641–648.
18. Fujita, N.; Ohmura, K.; Kikuchi, M.; Suzuki, T.; Funaki, S.; Hiroshige, I. Effect of Nb on high-temperature properties for ferritic stainless steel. *Scr. Mater.* **1996**, *35*, 705–710. [CrossRef]
19. Cheng, X.W.; Jiang, Z.Y.; Monaghan, B.J.; Longbottom, R.J.; Wei, D.B.; Hee, A.C.; Jiang, L.Z. Degradation of ferritic stainless steels at 1200 °C in air. *Mater. Corros.* **2018**, *69*, 63–75. [CrossRef]
20. Teng, S.; Qian, Z. Study on the high-temperature oxidation resistance of ultra-pure ferrite stainless steel. *Gansu Metall.* **2022**, *44*, 53–55.
21. Qin, Z.; Taosha, L.; Wen, W.; Langlang, Z.; Yuefeng, J. High temperature oxidation kinetics and evolution of oxide film structure of nanocrystalline Ni-12Cr alloy at 800 °C. *Chin. J. Corros. Prot.* **2022**, *42*, 733–742.
22. Chen, X.; Xiaochun, W.; Na, M.; Qianliang, S. 3DAP Study on the C Segregation Behavior of High Carbon High Alloy Steel During Deep Cooling Treatment. *J. Met.* **2015**, *51*, 325–332.
23. Huang, Z.; Yang, Y. The effect of niobium titanium on the high-temperature precipitation behavior of the second phase in ferritic stainless steel. *Met. Heat Treat.* **2015**, *40*, 7–12.
24. Xin, Z.; Wei, D.; Xunzheng, H. The effect of niobium titanium on the second phase precipitation and mechanical properties of 430 ferrite stainless steel. *Baosteel Technol.* **2015**, 6–12.
25. Chen, Y.; Zhan, J.; Ni, Q.; Li, M. Oxidation Behavior of 441 Ferritic Stainless Steel in Simulated Automotive Exhaust Gas Environment. *Corros. Sci. Prot. Technol.* **2019**, *31*, 174–180.
26. Zhao, T.; Teng, L.; Jin, Y.; Zhang, J.; Yang, Y. Microstructure and mechanical properties of niobium containing ferritic stainless steel suitable for automotive exhaust manifolds. *Shanghai Met.* **2020**, *42*, 63–68.
27. Hou, Q.; Jing, D.; Liao, Z.; Wang, K.; Xi, B.; Huang, Z. Effect of niobium on oxidation weight gain of 65SiCrV6 spring steel. *Steel* **2022**, 1–15.
28. Duan, X.; Zhang, J.; Wang, B.; Li, G. Behavior of Trace Elements during High Temperature Oxidation of 444 Ferritic Stainless Steel. In Proceedings of the 13th China Steel Annual Conference-7. Advanced Steel Materials and Their Applications, Online, 23–24 November 2022; pp. 443–449.